J Therm Anal Calorim (2013) 113:231–238
DOI 10.1007/s10973-013-3097-0

Practical remarks concerning phase diagrams determination on the basis of differential scanning calorimetry measurements

Leszek Rycerz

Received: 15 October 2012 / Accepted: 21 February 2013 / Published online: 26 March 2013

Phase diagrams of binary systems at constant pressure are representations of one- and two-phase regions with their boundaries being functions of temperature and concentration. The most popular techniques used in determination of phase diagrams are thermal analysis (TA), differential thermal analysis (DTA) and differential scanning calorimetry (DSC). The first of them, based on recording of cooling curves, has no significant meaning nowadays; however, it is still used, especially in didactics. Actually DTA and DSC are widely used in phase diagrams determination. DSC has an advantage over DTA, because in addition to temperature it gives precise value of enthalpy of thermal effect. Two types of DSCs must be distinguished: the heat flux DSC and the power compensation DSC.

The characteristic feature of all DSC measuring systems is the twin-type design and the direct in-difference connection of the two measuring systems which are of the same kind. It is the decisive advantage of the differential principle that, in first approximation, disturbances such as temperature variations in the environment of the measuring system and the like, affect the two measuring systems in the same way and are compensated when the difference between the individual signals is formed [1]. The differential signal is the essential characteristic of each DSC. Another characteristic—which distinguishes it from most classic calorimeters—is the dynamic mode of operation. The DSC can be heated or cooled at a preset heating or cooling rate. A characteristic common to both types of DSC is that the measured signal is proportional to a heat flow rate (in opposition to classical calorimeters where heat flow is measured). This fact—directly measured heat flow rates—enables the DSC to solve problems arising in many fields of application [1]. In the heat flux DSC a defined exchange of the heat to be measured takes place via a thermal resistance. The measurement signal is the temperature difference; it describes the intensity of the exchange and is proportional to the heat flow rate. There are two main types of the heat flux DSC: the disc-type measuring system with solid sample support (disc) and the cylinder-type measuring system with integrated sample cavities. Heat flux DSCs with a disc-type measuring system are available for temperatures between −190 and 1,500 °C [1]. In the heat flux DSC with a cylinder-type measuring system, the outer surfaces of each sample container are in contact with a great number of thermocouples connected in a series between the container and furnace cavity. The thermocouples bands or wires are the dominating heat conduction path from the furnace to samples. Both sample containers are thermally decoupled; heat exchange takes place only with parts of the massive furnace. These apparatuses are available for temperature range between −190 and 1,500 °C [1]. The power compensation DSC belongs to the class of heat-compensating calorimeters. The heat to be measured is compensated with electric energy, by increasing or decreasing an adjustable Joule's effect. The measuring temperature range extends from −175 to 725 °C [1].

Differential scanning calorimetry is a relative technique. Because of its dynamic temperature characteristics, the measurements are not made in thermal equilibrium. The relative data must be converted to absolute values by a calibration procedure requiring the employment of standards whose property values and their associated uncertainties are known and established following a metrological procedure [2].

Practical remarks concerning phase diagrams determination on the basis of DSC measurements are illustrated by numerous examples of binary lanthanide halide–alkali halide systems.

L. Rycerz (✉)
Chemical Metallurgy Group, Faculty of Chemistry, Wroclaw University of Technology, Wrocław, Poland
e-mail: leszek.rycerz@pwr.wroc.pl

Results presented in this work were obtained with Setaram DSC 121, which is a cylinder-type scanning calorimeter. Its temperature scale was calibrated in accordance with calibration procedure recommended by IUPAC Technical Report concerning calibration standards for DSC [2]. Temperature correction coefficients were calculated and subsequently used by apparatus software. Enthalpy calibration was performed by the so-called 'Joule effect'. Identical, standard-heating elements (resistivity of each equal 100 Ω) placed in alumina protection tubes were introduced into a constant temperature zone of the calorimetric block. One of them generated thermal impulses (P) of 200 mW during 200 s. Each impulse was followed by stabilization of calorimeter during 600 s. A computer recorded the value of the thermal effect (Q) introduced into calorimeter. The value of calorimeter constant K at temperature T is described by an equation:

$$K = \frac{\mathrm{Q}}{P \times t}.$$

Such calibration was carried out at defined temperatures by the so-called 'step method' ($\Delta T = 5$ K) over the entire temperature range of calorimeter work. As a result the calibration curve, *i.e.* calorimeter constant dependence on temperature, $K(\mu\mathrm{V\ mW^{-1}}) = f(T)$, was obtained. This dependence was automatically used during data treatment by original software of SETARAM. The maximum of relative error of enthalpy of phase transition determination did not exceed 1 %. Calibration of apparatus by 'Joule effect' was checked by measurements of temperatures and enthalpies of phase transitions of standard substances. Results obtained (differences in fusion temperatures less than 1 K, differences in enthalpies of fusion less than 0.5 %) confirmed correct work of calorimeter.

Temperatures of the invariant points were determined as T_{onset}, temperature of liquidus was determined as T_{peak}.

Unfortunately, enthalpy obtained in DSC measurements tell us nothing about the kind of reaction by which it is generated. Therefore, DSC technique must be supported by additional technique such as X-ray crystallography. A further development is the application of high-temperature X-ray techniques. Other methods applied in phase diagram determinations are high-temperature microscopy, measurement of electrical conductivity and metallographic methods (in case of alloys).

The correct phase diagram determination depends on many factors. Of course the method used is important, but primarily it depends on purity of components, proper preparation of the samples, correct measurements and analysis of obtained data, and supplementary methods such as for example X-ray diffraction. Lets assume that all other requirements for correct phase diagram determination are fulfilled and only correct analysis of DSC curves should be done.

In general one can observe characteristic dependence between topology of phase diagram and shape of DSC curves. Let us take the phase diagram of the binary system with incongruently melting compound (Fig. 1). If pure components undergo only melting one peak on DSC curve will be observed. It will be less or more unsymmetrical and return to base line will appear after it. For isopleth b two thermal effects will be observed on DSC heating curve. The first corresponding to incongruent melting and second one, with characteristic shape of longer or shorter tail, corresponding to the liquidus. For sample with composition c three effects related to eutectic, incongruent melting and liquidus will appear. Due to physical reasons return to the

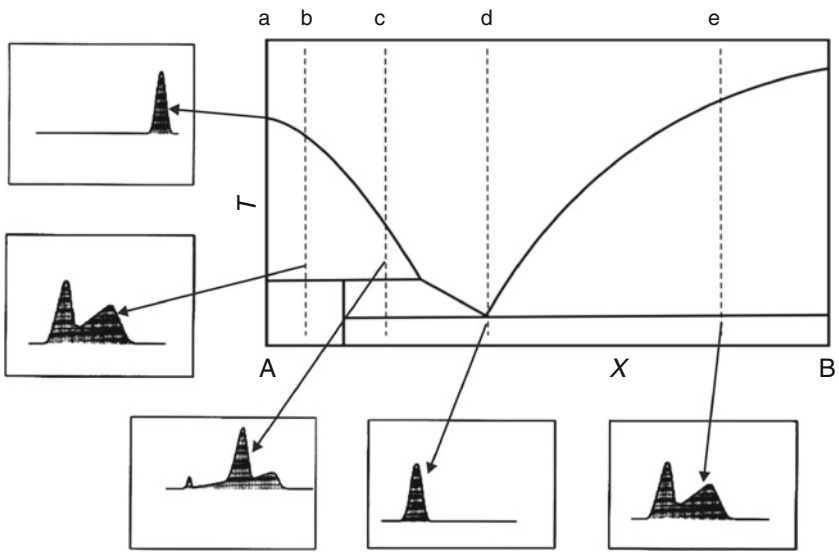

Fig. 1 Correlation between topology of phase diagram and shape of DSC curves

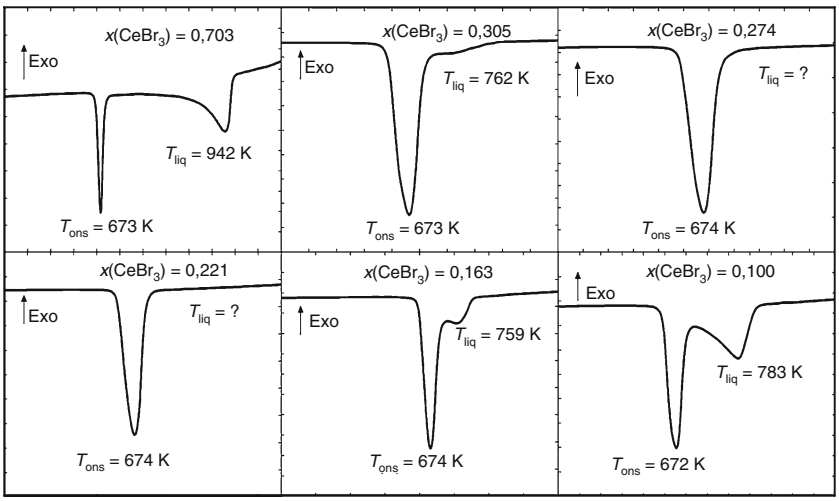

Fig. 2 DSC curves for the system $CeBr_3$–LiBr

baseline will take place after liquidus effect. The shape of pure eutectic effect (*d*) is identical to those of pure components. Finally for the sample with mole fraction *e* two peaks, related to eutectic and liquidus, will be present on DSC curve. Now let us look on real DSC curves for the $CeBr_3$–LiBr system (Fig. 2) [3]. Looking on the shape of DSC curves one can conclude that it is simple eutectic system. Two peaks are observed in almost all thermograms. The first at constant temperature (672–674 K) is undoubtedly related to the eutectic. The second one, with characteristic tail shape, corresponds to the liquidus. It is well visible for compositions far away from eutectic composition. For samples with compositions mowing to the eutectic composition it starts to be more close to the eutectic effect and less visible. Finally, for some compositions around eutectic (Fig. 2—molar fraction of $CeBr_3$ ranging from 0.274 up to 0.220) it is so small that it is not visible in DSC curves. Conclusion coming from such results is clear. It is impossible to determine eutectic composition directly from experimental curves. However, eutectic has strictly defined composition and cannot be situated at different mole fractions. Should the eutectic composition be taken randomly from the range of compositions where liquidus effect is not visible? Of course, not. Proper determination of eutectic composition requires creation of the so-called Tammann diagram, i.e. dependence of molar enthalpy related to the eutectic effect on mole fraction. As a consequence of the lever rule and the fact that it is always the same liquid that is initially formed (with the eutectic composition), the size of the integrated eutectic signal ($\Delta_r H$) should descend linearly by mole fraction on either side of the eutectic point. This is the basis for the Tammann diagram [4, 5].

The Tammann plot should start at whatever the left and the right endpoints of the eutectic line are. This only corresponds to $x = 0$ and $x = 1$ if the left and right phases have negligible solid solubility. This means that the plot can give us information on both the eutectic composition and the solid solubilities at T_{eutectic}. (The latter are typically the maximum solubilities). Results for the $CeBr_3$–LiBr system (Tammann diagram and phase diagram) are presented in Fig. 3. The intercept of straight lines in Tammann diagram gives mole fraction of $CeBr_3$, $x(CeBr_3) = 0.249$ for eutectic composition. These lines cross the composition axis at $x(CeBr_3) = 0$ and 1. This means that the formation of solid solutions on both sides of the system is negligible.

Tammann plot constructed for the $YbCl_2$–NaCl system (Fig. 4) gives information about eutectic composition [$x(YbCl_2) = 0.559$] and informs about formation of solid solution of $YbCl_2$ in NaCl [6]. Limit of solubility at eutectic temperature corresponds to mole fraction of $YbCl_2$ equal 0.123.

Tammann diagram can be also used for determination of stoichiometry of incongruently melting compound. Figure 5 presents phase diagram of $TbBr_3$–RbBr binary system [7] and Tammann diagram used for determination of TbBr–Rb_3TbBr_6 eutectic composition and stoichiometry of incongruently melting $RbTb_2Br_7$ compound. Mole fraction of $TbBr_3$, $x(TbBr_3) = 0.658$ is in quite good agreement with

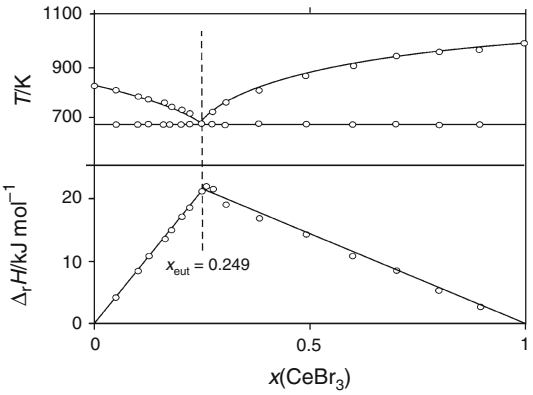

Fig. 3 Tamman and phase diagrams for the $CeBr_3$–LiBr system [3]

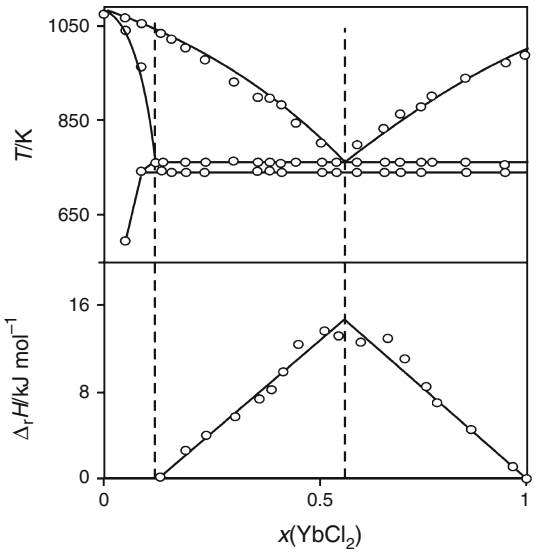

Fig. 4 Tamman and phase diagrams for the $YbCl_2$–NaCl system

theoretical value (0.666) corresponding to the stoichiometry of $RbTb_2Br_7$ compound.

Sometimes it is difficult or even impossible to create Tammann diagram. Such a situation takes place in the case of determination of Rb_3TbBr_6–$RbTb_2Br_7$ eutectic composition (Fig. 5) [7]. In the very narrow temperature range 712–728 K, several phase equilibria take place over the whole composition range. However, their number is difficult to appreciate over the composition range $0.250 < x(TbBr_3) < 0.666$. For this reason more detailed investigations on this composition range were performed by running DSC scans at far smaller heating rates (1 and 0.2 K min^{-1}). Indeed the thermal events merged in Fig. 6 a, b) were deconvoluted upon slower heating at 1 K min^{-1} (Fig. 7a) and even revealed more details at 0.2 K min^{-1} (Fig. 7b, c).

For mixtures in the composition range $0.250 < x(TbBr_3) < 0.445$, an additional effect at 718 K was visible in addition

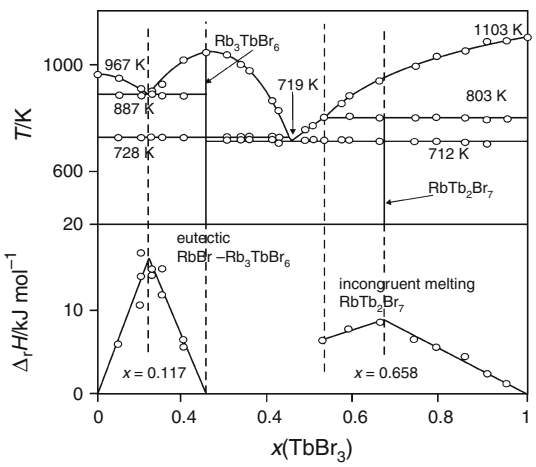

Fig. 5 Tamman and phase diagrams for the $TbBr_3$–RbBr system [7]

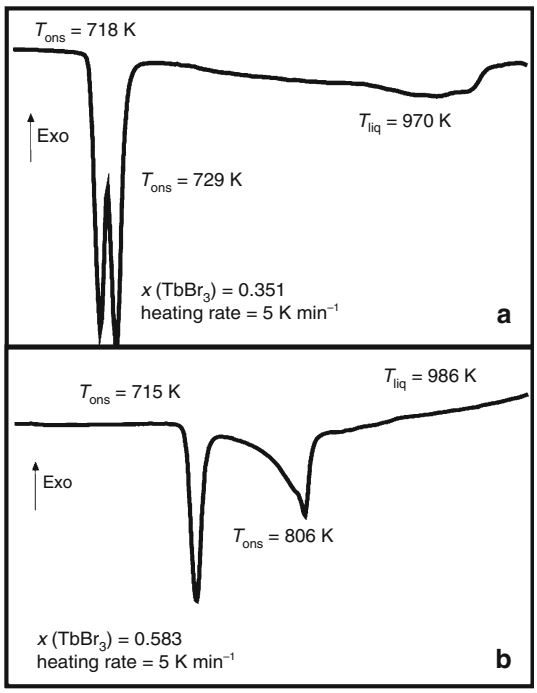

Fig. 6 DSC heating curves for selected xTbBr$_3$–$(1 - x)$RbBr mixtures ($x = 0.351$ and 0.583)

to the liquidus and Rb_3TbBr_6 transition at 728 K but merged with the latter under standard heating conditions (5 K min^{-1}). In an attempt to separate these events, further experimentation was performed at slower heating rates [7]. While at 1 K min^{-1} the phase transition occurred separately, the anticipating effect at 718 K was found to be superimposition of two effects and could not be fully resolved even upon very slow heating (0.2 K min^{-1}), as shown in Fig. 7b. However, even so, two characteristic temperatures (712 and 719 K) were determined in all samples in the composition range $0.25 < x(TbBr_3) < 0.666$ and only one (712 K) at compositions beyond. Effect at 712 K was assigned to the solid–solid transition of the $RbTb_2Br_7$ compound. Accordingly the thermal event at 719 K should be related to the formation of a eutectic mixture of Rb_3TbBr_6 and $RbTb_2Br_7$. The evaluation of this eutectic mixture composition from an enthalpy versus composition plot, as explained above, would not be reliable in view of the merged and non-separable enthalpy effects observed in the narrow temperature range 712–719 K. An alternate method was used instead. The global enthalpy related to the overlapping effects, ΔH_m (global), was determined from DSC thermograms obtained at heating rate of 5 K min^{-1}. The enthalpy related to the eutectic, ΔH_m (eutectic) can be calculated as:

$$\Delta H_m(\text{eutectic}) = \Delta H_m(\text{global}) - \Delta_{trs}H_m(Rb_3TbBr_6) - \Delta_{trs}H_m(RbTb_2Br_7).$$

The contribution of the enthalpy of transition, $\Delta_{trs}H_m$ (Rb_3TbBr_6 solid–solid transition), to the global enthalpy could be determined from a Tammann diagram as shown in

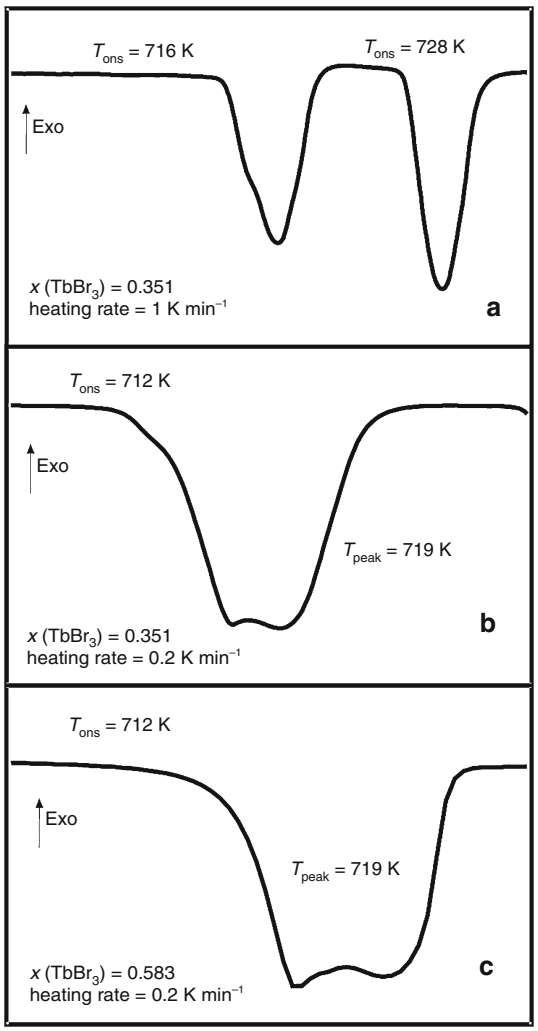

Fig. 7 DSC heating curves for selected $x TbBr_3$–$(1 - x)$RbBr mixtures ($x = 0.351$ and 0.583)

Fig. 8a. The effect at 728 K only results from the solid–solid phase transition in Rb_3TbBr_6 at $x(TbBr_3) \leq 0.25$ (Fig. 5) and the related enthalpy varies linearly with composition with the maximal value 1.974 kJ mol^{-1} at $x(TbBr_3) = 0.25$. The linear dependence must occur also for $x(TbBr_3) > 0.25$. The thermal effect related to this transition disappears at $x(TbBr_3) \sim 0.445$, thus at $x(TbBr_3) = 0.445$ this enthalpy must be 0. Using the enthalpy values at $x(TbBr_3) = 0.25$ (1.974 kJ mol^{-1}) and $x(TbBr_3) = 0.445$ (0 kJ mol^{-1}) (black circles in Fig. 8a) $\Delta_{trs}H_m$ (Rb_3TbBr_6) was fitted to the linear equation ($0.25 \leq x(TbBr_3) \leq 0.445$) and plotted against $x(TbBr_3)$ in Fig. 8a (dashed line). The contribution of $\Delta_{trs}H_m$ ($RbTb_2Br_7$) to the global enthalpy was described in a similar way (Fig. 8c). The thermal effect at 712 K only results from the solid–solid phase transition in $RbTb_2Br_7$ at $0.666 \leq x(TbBr_3) < 1$ (Fig. 5). The corresponding enthalpy is a linear function of $x(TbBr_3)$ with the maximal value 5.453 kJ mol^{-1} at $x(TbBr_3) = 0.666$. The thermal effect related to this

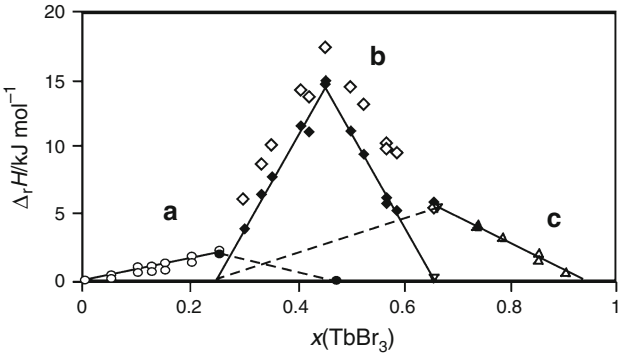

Fig. 8 Graphical evaluation of the thermal effect related to Rb_3TbBr_6–$RbTb_2Br_7$ eutectic: *open circles* enthalpy related to the Rb_3TbBr_6 transition at 728 K (*a*), *open triangles* enthalpy related to the $RbTb_2Br_7$ transition at 712 K (*c*), *open diamonds* global enthalpy in composition range $0.25 \leq x \leq 0.666$, *black diamonds* enthalpy related to the Rb_3TbBr_6–$RbTb_2Br_7$ eutectic with $T_{eut} = 718$ K (*b*)

transition disappears at $x(TbBr_3) = 0.25$ thus at $x(TbBr_3) = 0.25$ this enthalpy must be 0. The enthalpy values at $x(TbBr_3) = 0.25$ (0 kJ mol^{-1}) and $x(TbBr_3) = 0.666$ (5.453 kJ mol^{-1}) (black triangles in Fig. 8c) resulted in the linear equation of the $\Delta_{trs}H_m$ ($RbTb_2Br_7$) in the molar fraction range $0.25 \leq x(TbBr_3) \leq 0.666$ as displayed in Fig. 8c (broken line). It was then possible to calculate the enthalpy change related to the Rb_3TbBr_6–$RbTb_2Br_7$ eutectic (Fig. 8b). The eutectic composition [$x(TbBr_3) = 0.449$] was determined from the intercept of the two linear parts in Fig. 8b.

Sometimes very interesting phenomena in form of exo-effects are observed on DSC curves. Such a situation was observed in the $CeBr_3$–CsBr system [8]. Phase diagram of this system is presented in Fig. 9. For samples with composition $0.250 < x(CeBr_3) < 0.666$ (Fig. 9) on primary heating curves (heating rate 5 K min^{-1}), an endothermic effect was visible at 685 K at all compositions, which was assessed to possible decomposition of Cs_2CeBr_5 into the adjacent Cs_3CeBr_6 and $CsCe_2Br_7$ compounds. However, on subsequent cooling, the formation of Cs_2CeBr_5 was not observed (Fig. 10a) and it is likely that a metastable mixture

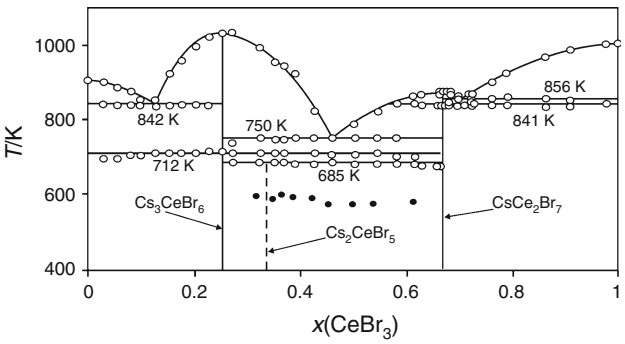

Fig. 9 Phase diagram of the CsBr–$CeBr_3$ system [8]

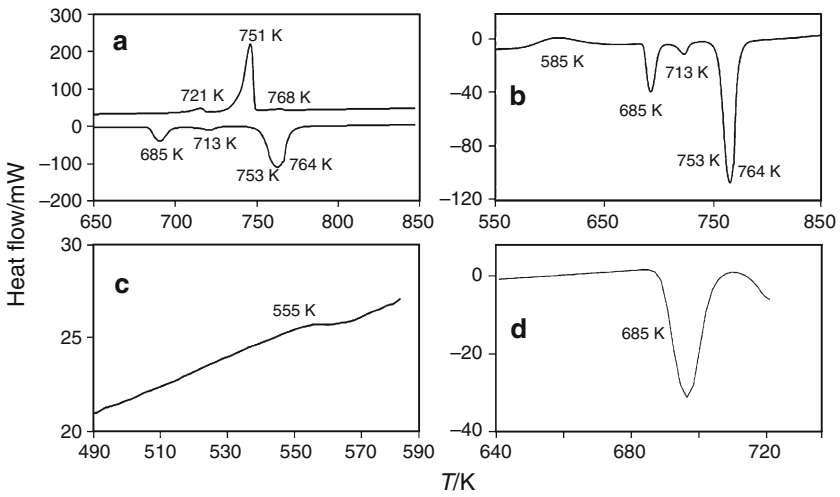

Fig. 10 Experimental curves [8]: **a** primary heating/cooling (5 K min^{-1}); **b** secondary heating (5 K min^{-1}); **c** Cs_3CeBr_5 formation on slow cooling (0.1 K min^{-1}); **d** subsequent heating

of Cs_3CeBr_6 and $CsCe_2Br_7$ exists down to room temperature instead. Solid-state reactions, such as the formation or decomposition of compounds in the solid state, can be considered as a special kind of reconstructive transition in which the arrangement of the ions is drastically changed. Ions have to move from one site to another passing strong potential walls of other ions. The resulting 'kinetic hindrance' can cause a great difference between reaction temperatures, measured in DSC heating and cooling runs (thermal hysteresis) [9]. In extreme cases during cooling experiments the 'undercooling' can become so strong that the reaction does not occur in the DSC time-scale. Due to kinetic reasons, the compound formation during cooling does not take place and a metastable mixture of other compounds exists instead. Thus secondary heating runs were performed at heating rate 5 K min^{-1} and this time an exothermic effect was observed first at about 585 K which was followed by an endothermic effect (Fig. 10b) occurring at a temperature identical to that of decomposition previously observed (685 K). But on this secondary cooling curve, the effect at 685 K (compound formation) was once again not visible. So, we decided to heat once again one sample up to melting and to cool it down to room temperature, but at a very low cooling rate (0.1 K min^{-1}). This time the effect corresponding to the compound formation was observed at about 655 K (Fig. 10c). As the compound was formed during cooling, no exothermic effect was present in subsequent heating DSC curve (Fig. 10d).

Another problem with interpretation of DSC curves arises sometimes in the case of existence of incongruently melting compounds [10]. This difficulty can be exemplified by the phase diagram of $DyBr_3$–RbBr system (Fig. 11) [11]. Because of the large temperature difference of the melting point of Rb_3DyBr_6 (1,059 K) and the potential eutectic formed by Rb_2DyBr_5 compound (about 700 K) during cooling a large amount of Rb_3DyBr_6 crystallizes from the melt above the temperature incongruent melting of Rb_2DyBr_5 (presumably 734 K). The crystals separate from the melt and, therefore, the formation of Rb_2DyBr_5 is not complete. As a consequence, all other effects at lower temperatures, namely the eutectic and phase transition of Rb_3DyBr_6 will appear also in the range of compositions where the above-mentioned temperature difference is large. Thus, the quenched samples have to be annealed to get equilibrium conditions [10]. We have performed the annealing of the samples with molar fraction of the $DyBr_3$ ranging from 0.25 to 0.40 at temperature 708 K during 78 h. The curves of the samples with $x(DyBr_3) = 0.283$ and $x(DyBr_3) = 0.376$ without annealing and after annealing, obtained with heating rate 1 K min^{-1}, are presented in Fig. 12.

For the samples with molar fraction $x(DyBr_3) < 0.333$ effect at about 700 K (potentially related to the Rb_2DyBr_5 eutectic) disappears (Fig. 12a, b). For the samples with molar fraction $x(DyBr_3) > 0.333$ disappears effect at temperature of about 717 K (Fig. 12c, d) corresponding to the

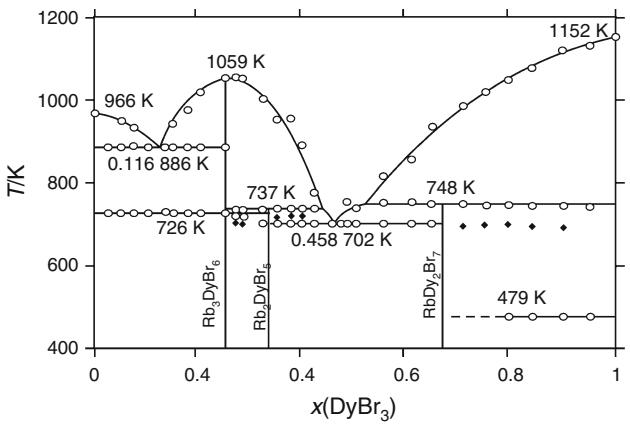

Fig. 11 Phase diagram of $DyBr_3$–RbBr system [11]: *black diamonds* additional effects that were observed in DSC curves obtained for samples without annealing

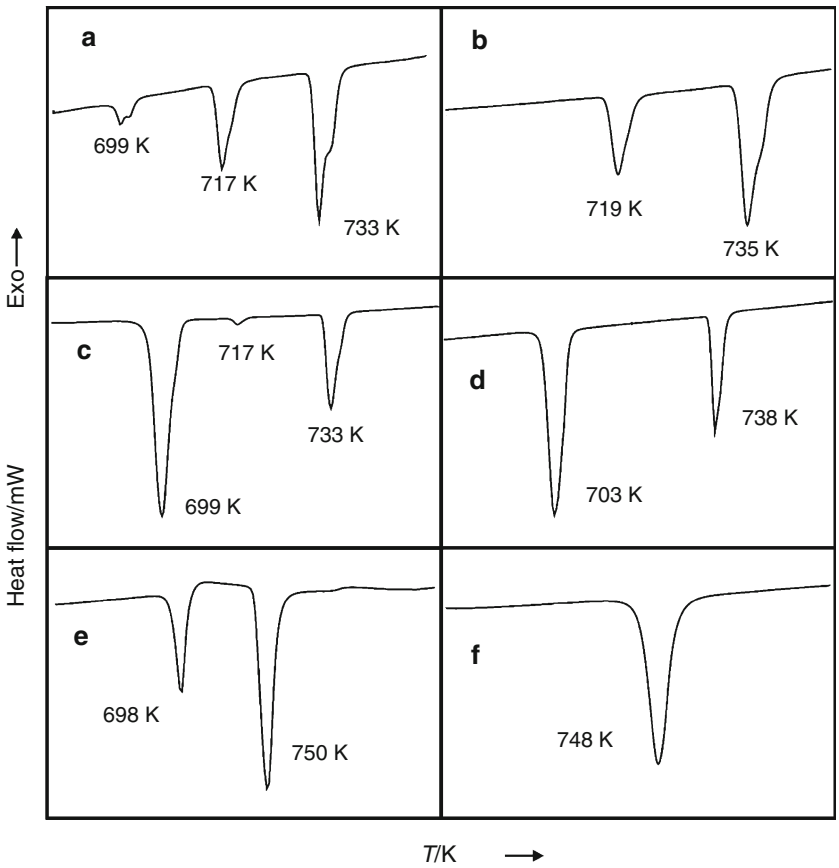

Fig. 12 DSC heating curves for $DyBr_3$–RbBr [11] without (*a*, *c*, *e*) and after (*b*, *d*, *f*) annealing at 708 K during 48 h: (*a*, *b*) $x = 0.283$; (*c*, *d*) $x = 0.376$; (*e*, *f*) $x = 0.706$. Heating rate 1 K min^{-1} (indicated temperatures are onset temperatures)

phase transition of Rb_3DyBr_6. These annealing experiments confirmed existence of incongruent melting at 737 K (mean value from all appropriate curves) Rb_2DyBr_5 compound. Effect at lower temperature (702 K) is related to the eutectic formed by Rb_2DyBr_5.

In the composition range $0.50 < x(DyBr_3) < 1.00$ two endothermic peaks were present in all heating curves in addition to liquidus. The temperature of first effect corresponds very well with effect observed for samples with molar fraction of $DyBr_3$ $0.33 < x(DyBr_3) < 0.50$ (about 702 K). The second effect occurs at about 750 K and suggests existence of another incongruently melting compound. However, existence of this compound should influence effect at lower temperature (702 K). At composition of this compound effect at 702 K, related to the eutectic, should disappear. But once again we have the situation of large difference between melting temperature of $DyBr_3$ (1,152 K) and temperature of incongruent melting of this hypothetical compound (750 K). Annealing of the samples was performed at 708 K during 78 h. As a result of this annealing the thermal effect at 702 K disappeared in the samples with $x(DyBr_3) > 0.666$ (Fig. 12e, f), thus confirming existence of $RbDy_2Br_7$ incongruently melting compound.

Conclusions

1. There is a characteristic dependence between topology of phase diagram and shape of DSC curves.
2. Tammann diagram is outcome from the theory of phase diagrams and predicts, through application of the lever rule the variation of enthalpy associated with a first-order transformation as a function of concentration. Regrettably, this plot is seldom used or merely overlooked, although it provides valuable information and is known from beginning of XX century.
3. 'Kinetic hindrance' which can appear in the case of solid-state reactions, such as the formation or decomposition of compounds in the solid state, can lead to the metastable phases formation.
4. Existence of incongruently melting compounds can cause difficulties with interpretation of DSC curves. Because of the large temperature difference of the melting point of neighbouring congruently melting compound and eutectic, during cooling a large amount of this congruently melting compound crystallizes from the melt above the temperature of incongruent melting. The crystals separate from the melt and,

therefore, the formation of incongruently melting compound is not complete. As a consequence, all other effects at lower temperatures will appear also in the range of compositions where the above-mentioned temperature difference is large. Thus, the quenched samples have to be annealed to get equilibrium conditions.

Acknowledgments The work was financed by a statutory activity subsidy from the Polish Ministry of Science and Higher Education for the Faculty of Chemistry of Wroclaw University of Technology.

References

1. Hohne GWH, Hemminger W, Flammersheim HJ. Differential scanning calorimetry. An introduction for practitioners. Heidelberg: Springer; 1996.
2. Della Gatta G, Richardson MJ, Sarge SM, Stolen S Standards. Calibration and guidelines in microcalorimetry. Part 2. Calibration standards for differential scanning calorimetry (IUPAC technical report). Pure Appl Chem. 2006;78(7):1455–76.
3. Ingier-Stocka E, Rycerz L, Gadzuric S, Gaune-Escard M. Thermal and conductometric studies of the $CeBr_3$–MBr binary systems (M=Li, Na). J Alloys Comp. 2008;450:162–6.
4. Findlay A. The phase rule and its applications. New York: Longmans, Green and Co.; 1911.
5. Guenet JM. Contributions of phase diagrams to the understanding of organized polymer-solvent systems. Thermochim Acta. 1996; 284:67–83.
6. Rycerz L. Phase diagram of the $YbCl_2$–NaCl binary system (unpublished results).
7. Rycerz L, Gaune-Escard M. Phase diagram of the $TbBr_3$–RbBr binary system: thermodynamic and transport properties of the Rb_3TbBr_6 compound. Inorg Chem. 2007;46:2299–306.
8. Rycerz L, Ingier-Stocka E, Gaune-Escard M. Phase diagram and electrical conductivity of the $CeBr_3$–CsBr binary system. J Therm Anal Calorim. 2009;97:1015–21.
9. Seifert HJ. Ternary chlorides of the trivalent late lanthanides. J Therm Anal Calorim. 2006;83:479–505.
10. Sebastian J, Seifert HJ. Ternary chlorides in the systems ACl/YbCl3 (A=Cs, Rb, K). Thermochim Acta. 1998;318:29–37.
11. Chojnacka I, Rycerz L, Berkani M, Gaune-Escard M. Phase diagram and electrical conductivity of the $DyBr_3$–RbBr binary system. J Therm Anal Calorim. 2012;108(2):481–8. doi:10.1007/s10973-011-2017-4.